

Pressure Dependence of Superconducting Properties, Pinning Mechanism, and Crystal Structure of the $\text{Fe}_{0.99}\text{Mn}_{0.01}\text{Se}_{0.5}\text{Te}_{0.5}$ Superconductor

Kannan Murugesan, Govindaraj Lingannan, Kento Ishigaki, Yoshiya Uwatoko, Chihiro Sekine, Yukihiro Kawamura, Hayashi Junichi, Bobby Joseph, Ponniah Vajeeston, Pankaj Kumar Maheswari, V. P. S. Awana, and Arumugam Sonachalam*



Cite This: *ACS Omega* 2021, 6, 30419–30431



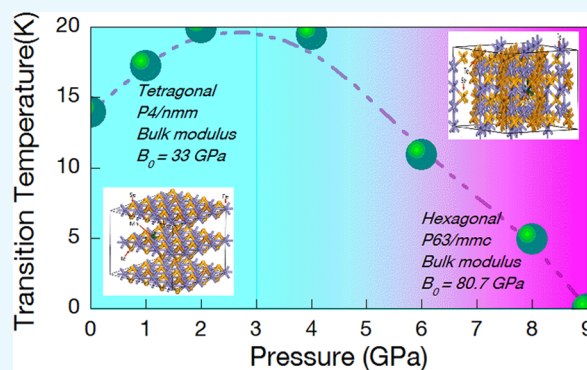
Read Online

ACCESS |

Metrics & More

Article Recommendations

ABSTRACT: We have investigated the pressure (P) effect on structural (up to 10 GPa), transport [$R(T)$: up to 10 GPa], and magnetic [$M(T)$: up to 1 GPa] properties and analyzed the flux pinning mechanism of the $\text{Fe}_{0.99}\text{Mn}_{0.01}\text{Se}_{0.5}\text{Te}_{0.5}$ superconductor. The maximum superconducting transition temperature (T_c) of 22 K with the P coefficient of T_c $dT_c/dP = +2.6$ K/GPa up to 3 GPa ($dT_c/dP = -3.6$ K/GPa, $3 \leq P \leq 9$ GPa) was evidenced from $R(T)$ measurements. The high-pressure diffraction and density functional theory (DFT) calculations reveal structural phase transformation from tetragonal to hexagonal at 5.9 GPa, and a remarkable change in the unit cell volume is observed at ~ 3 GPa where the T_c starts to decrease, which may be due to the reduction of charge carriers, as evidenced by a reduction in the density of states (DOS) close to the Fermi level. At higher pressures of $7.7 \text{ GPa} \leq P \leq 10.2 \text{ GPa}$, a mixed phase (tetragonal + hexagonal phase) is observed, and the T_c completely vanishes at 9 GPa. A significant enhancement in the critical current density (J_c) is observed due to the increase of pinning centers induced by external pressure. The field dependence of the critical current density under pressure shows a crossover from the δl pinning mechanism (at 0 GPa) to the δT_c pinning mechanism (at 1.2 GPa). The field dependence of the pinning force at ambient condition and under pressure reveals the dense point pinning mechanism of $\text{Fe}_{0.99}\text{Mn}_{0.01}\text{Se}_{0.5}\text{Te}_{0.5}$. Moreover, both upper critical field (H_{c2}) and J_c are enhanced significantly by the application of an external P and change over to a high P phase (hexagonal ~ 5.9 GPa) faster than a $\text{Fe}_{0.99}\text{Ni}_{0.01}\text{Se}_{0.5}\text{Te}_{0.5}$ (7.7 GPa) superconductor.



INTRODUCTION

The discovery of superconductivity in iron selenide (α -FeSe) with $T_c = 7 \text{ K}$ ¹ has gained considerable attraction after cuprates^{2,3} and iron arsenides^{4,5} because of their simple crystal structure. The iron-based superconductors (SCs) are the most promising materials for high-magnetic-field applications due to their large T_c , J_c , and H_{c2} and low anisotropy.^{6–13} The binary FeSe_{1-x} system in which Se deficiency stabilizes the superconductivity has a similar structure to that of iron pnictide (Fe-As) SCs.^{4,5} The Fe-Se layer plays a key role in the appearance of superconductivity in Fe-Se-based SCs¹ like the Fe-As layer in 1111 and 122 iron pnictide series.^{14,15} Te substitution in Se sites raises the T_c from 7 to 14 K in $\text{FeSe}_{0.5}\text{Te}_{0.5}$.^{16,17} Addition of metallic elements (MEs) in Fe sites of $\text{FeSe}_{0.5}\text{Te}_{0.5}$ ($\text{Fe}_{1-x}\text{ME}_x\text{Se}_{0.5}\text{Te}_{0.5}$) is also found to enhance the superconducting properties. For example, on Cr substitution of 1%, the T_c increased from 14 to 15.7 K.¹⁸ Further, in this case, the diamagnetic shielding fraction was improved and a very high

upper critical field ($H_{c2}(0) = 332$ to 1080 kOe) was observed.¹⁸ In Ag doping of 5%, even though the T_c decreased from 14 to 11 K, an excess amount of Ag induced a new pinning center with an enhancement of J_c (i.e., $J_c/J_c(0)$ is increased from 1 to 1.5).¹⁹ With a 5% Sn doping, T_c is increased from 9 to 15 K with a simultaneous structural phase change from the hexagonal phase to the tetragonal phase.²⁰ As compared with Cu substitution in $\text{Fe}_{1+y}\text{Te}_{0.6}\text{Se}_{0.4}$, Co doping increases the paramagnetic moments and magnetic moments with an increase in the doping level.²¹ Further, a doping effect is reported for the composition of $\text{Fe}_{0.95}\text{ME}_{0.05}\text{Te}_{0.8}\text{Se}_{0.2}$ (ME

Received: July 14, 2021

Accepted: October 25, 2021

Published: November 5, 2021



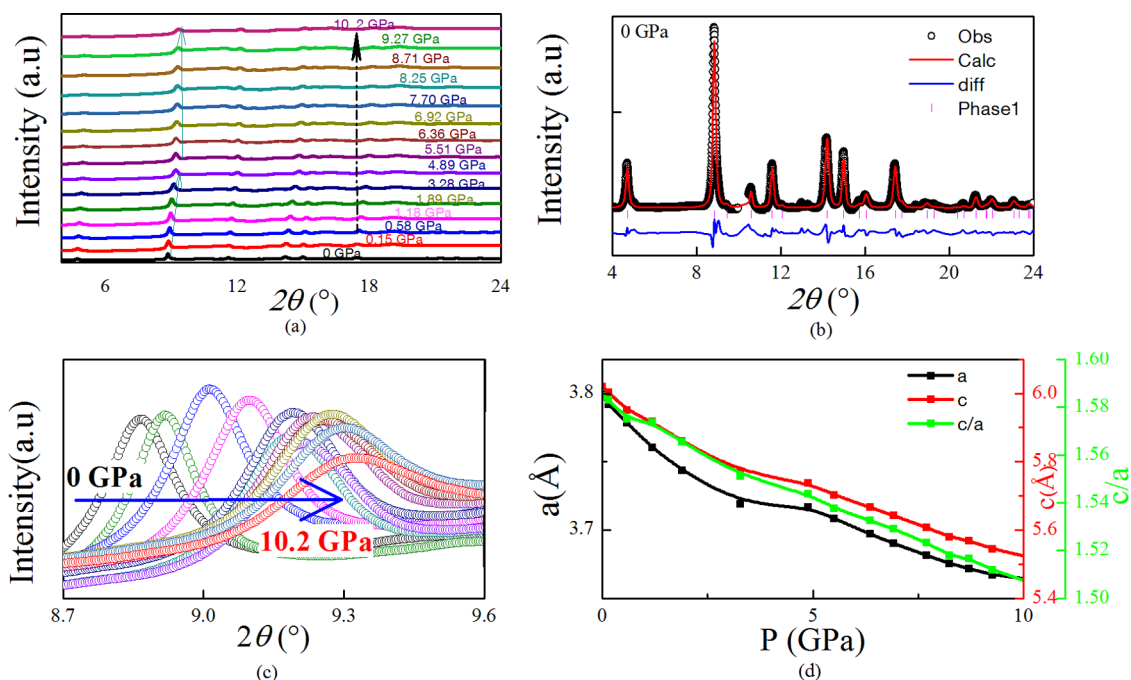


Figure 1. (a) Synchrotron powder X-ray diffraction pattern under pressure up to ~ 10 GPa for $\text{Fe}_{0.99}\text{Mn}_{0.01}\text{Se}_{0.5}\text{Te}_{0.5}$. (b) Powder X-ray diffraction pattern together with results of the Rietveld refinement at $P = 0$ GPa. (c) Expanded view of a particular 2θ peak from 0 to ~ 10 GPa (for the sake of clarity, some patterns are removed even though all of the peaks shift to the higher angle with application of P). (d) Pressure-dependent lattice parameters (a , c) and the c/a ratio under pressure up to ~ 10 GPa.

= Cr, Mn, Co, Ni, Cu, and Zn). It was found that Co, Ni, or Cu doping disfavors superconductivity, but Cr, Zn, and Mn doping favors it; however, only Mn doping shows a sharp superconducting transition.²² Moreover, with Co and Ni doping, both the Hall coefficient²³ and T_c decrease.²⁴ Both strong vortex pinning and high critical current density are required for various industrial applications of SC materials. Vortex pinning exhibits two types of pinning mechanisms: (i) δl , pinning due to the changes in the mean free path; and (ii) δT_c , spatial variation in the transition temperature. Flux pinning studies at 6 K suggest that δl pinning is dominant in FeSe ,²⁵ $\text{FeSe}_{0.5}\text{Te}_{0.5}$,²⁶ and $\text{Fe}_{0.97}\text{Co}_{0.03}\text{Se}_{0.5}\text{Te}_{0.5}$.²⁷ This may be due to changes in the mean free path along with J_c . Values of $J_c(0) \approx 5000$ and 15000 A/cm^2 at 6 K for $\text{FeSe}_{0.5}\text{Te}_{0.5}$ and $\text{Fe}_{0.97}\text{Co}_{0.03}\text{Se}_{0.5}\text{Te}_{0.5}$, respectively, have also been reported.

In addition to the doping of elements (chemical pressure), external pressure (P) is an effective way to enhance/decrease the SC properties by changing the structural parameters and pinning centers. Further, the external P reduces anisotropy by shrinking unit cells²⁸ and enhances the J_c by inducing more pinning centers.^{29,30} As far as the pressure effect is concerned, for β - FeSe , T_c increases (8.5 to 36.7 K under an applied P of 8.9 GPa) and then decreases at higher P followed by a decreasing trend, which is associated with the remarkable decrease in volume of the unit cell. It is due to the collapse of the space between the Fe_2Se_2 planes, and a phase transition occurs from the tetragonal to hexagonal phase.³¹ P dependence of T_c reported for $\text{Fe}_{1.03}\text{Se}_{0.57}\text{Te}_{0.43}$, and it is found that the T_c increases from 13.9 K (0 GPa) to maximum of 23.3 K (~ 3 GPa)³². Further, on compression above 11.9 GPa, a distorted monoclinic structure is observed, and it led to the suppression of superconductivity.³² Further, for $\text{FeSe}_{1-x}\text{Te}_x$ at $x = 0.5$, T_c (~ 14 K) is enhanced (27–37 K) by applying an external pressure.^{31,33–35} For the Co-doped sample, a significant

enhancement of T_c (from 11.5 to 17 K) and J_c has been reported up to 1.2 GPa.³⁶ Further, the P effect on the flux pinning mechanism has also been reported for $\text{Fe}_{0.97}\text{Co}_{0.03}\text{Se}_{0.5}\text{Te}_{0.5}$.³⁶

Generally, from the application point of view, SCs with high T_c , high J_c , and high H_{c2} are preferred; however, it is still a huge obstacle to enhancing the J_c along with vortex pinning and other superconducting properties. Evidently, the J_c , H_{c2} , and flux pinning were enhanced by both chemical and physical pressures on this iron-selenide system.^{25–27} The ionic radius of Mn is higher than that of Ni and also the $\text{Fe}_{0.99}\text{Ni}_{0.01}\text{Fe}_{0.5}\text{Te}_{0.5}$ sample to have a negative chemical pressure and the corresponding change in T_c . Further, it exhibits $dT_c/dP = +5$ K/GPa up to 3 GPa followed by a decrease of T_c and suppression at 10 GPa (quasi-hydrostatic pressure). Hence, we investigated the $\text{Fe}_{0.99}\text{Mn}_{0.01}\text{Fe}_{0.5}\text{Te}_{0.5}$ sample under a hydrostatic pressure of up to 12 GPa and compared the results with the Ni-doped one to understand the P dependence of T_c on both samples. In this context, the P effect on the pinning mechanism has been reported only for $\text{FeSe}_{0.5}\text{Te}_{0.5}$ and $\text{Fe}_{0.97}\text{Co}_{0.03}\text{Se}_{0.5}\text{Te}_{0.5}$ but not for Mn-doped $\text{FeSe}_{0.5}\text{Te}_{0.5}$. Hence, we investigated the SC properties and flux pinning properties of the $\text{Fe}_{0.99}\text{Mn}_{0.01}\text{Se}_{0.5}\text{Te}_{0.5}$ superconductor under an external P . Further, we also investigated the P and field dependence of the critical current density.

RESULTS AND DISCUSSION

Structural Properties of $\text{Fe}_{0.99}\text{Mn}_{0.01}\text{Se}_{0.5}\text{Te}_{0.5}$ under Pressure 10 GPa. The in situ powder X-ray diffraction data were collected at ambient pressure and various P (0–10 GPa) at RT in the ELETTRA synchrotron radiation Xpress beamline for the $\text{Fe}_{0.99}\text{Mn}_{0.01}\text{Se}_{0.5}\text{Te}_{0.5}$ sample, as shown in Figure 1a. Exploration of the diffraction profile shows a tetragonal structure (space group: $P4/nmm$) in the $\text{Fe}_{0.99}\text{Mn}_{0.01}\text{Se}_{0.5}\text{Te}_{0.5}$

superconductor at ambient P (see Figure 1b). The observed powder diffraction profiles under various P reveal that no structural change occurs and continue to exhibit tetragonal structures in the P range of 0.1–7.7 GPa. Further, a monotonic decrease of the lattice parameters until 3.28 GPa followed by a moderate decrease until 10 GPa (Figure 1d) and found a sudden change in the c/a ratio at 3.28 GPa (tetragonal cell parameters from 1.58456 to 1.54381 (2.4%)) (Figure 1d) and a 10% reduction in the volume at 3.28 GPa (Figure 2) as

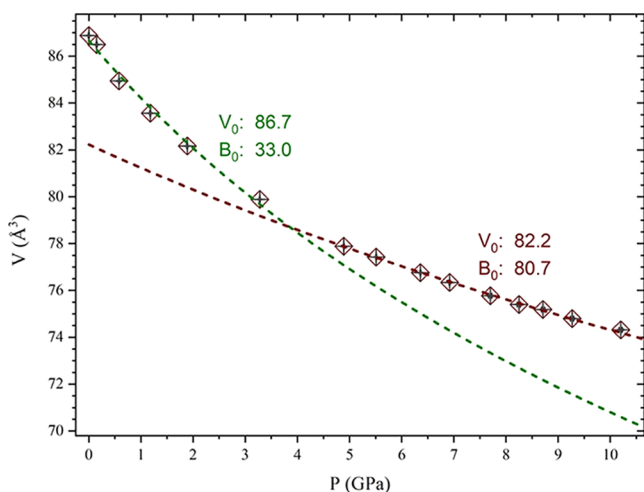


Figure 2. Pressure dependence of the unit cell volume up to ~10 GPa (which was extracted from high-pressure X-ray diffraction) for $\text{Fe}_{0.99}\text{Mn}_{0.01}\text{Se}_{0.5}\text{Te}_{0.5}$.

observed for $\text{Fe}_{0.99}\text{Mn}_{0.01}\text{Se}_{0.5}\text{Te}_{0.5}$. These results reveal a possible collapse of the van der-Waals-bonded region that separates Fe_2Se_2 planes, similar to structural studies reported for the FeSe compound.³⁷ Between 7.7 and 10.2 GPa, a more complicated structure is observed. At 7.7 GPa, the diffraction profile shows a partial transformation to a hexagonal NiAs-type structure—the same transformation reported for FeSe^{31,38} and also for $\text{Fe}_{0.99}\text{Ni}_{0.01}\text{Se}_{0.5}\text{Te}_{0.5}$ ³⁹ at different P . A characteristic first-order transition of mixed-phase (tetragonal + hexagonal) coexistence is seen in the wide P region: $5.9 \text{ GPa} \leq P \leq 10 \text{ GPa}$. It is noted that for FeSe the mixed phase started at 8.5 GPa and a complete transformation to the hexagonal phase was observed at 12 GPa.³⁷ However, the P dependence of lattice parameters was strongly anisotropic (a and c contract by

3.3 and ~8%, respectively), revealing a significant shrinkage in the interlayer spacing compared to the intralayer dimensions. As P increases, the c/a ratio smoothly decreases, as shown in Figure 1d. Further, in the P region 7.7–10 GPa shows a mixed phase. For the case of $\text{Fe}_{0.99}\text{Ni}_{0.01}\text{Se}_{0.5}\text{Te}_{0.5}$, the mixed phase was identified at 7.5 GPa, and at 15 GPa, the tetragonal structure was completely transformed to a hexagonal structure.³⁹ A close inspection shows that all of the peaks are shifted to a higher angle (Figure 1c), which reveals the reduction in the unit cell volume. Figure 2 shows the pressure dependence of the unit cell volume of $\text{Fe}_{0.99}\text{Mn}_{0.01}\text{Se}_{0.5}\text{Te}_{0.5}$. There is a discontinuous change in the unit cell volume between 3 and 4 GPa. The equation of state (EOS) fit to the data is undertaken with a second-order Birch–Murnaghan equation⁴⁰ as follows

$$P(V) = \frac{3}{2}B_0 \left[\left(\frac{V_0}{V} \right)^{7/3} - \left(\frac{V_0}{V} \right)^{5/3} \right] \quad (1)$$

where B_0 is the bulk modulus and V_0 is the unit cell volume at ambient pressure at *atm* conditions. The fittings yield $B_0 = 33 \text{ GPa}$ below 3.28 GPa and $B_0 = 80.7 \text{ GPa}$ above 3.28 GPa. The B_0 values we obtain are comparatively higher than those of FeSe^{34,38} and $\text{FeSe}_{0.5}\text{Te}_{0.5}$ ³² (30.9 and 36.6 GPa, respectively) in the tetragonal phase. In the pressure-released state (0.02 GPa), although the intensities are not restored, all Bragg peaks are almost reverted to their ambient P condition, thus showing the elasticity of $\text{Fe}_{0.99}\text{Mn}_{0.01}\text{Se}_{0.5}\text{Te}_{0.5}$.

DFT Calculations. The structural parameters of FeSe in the hexagonal and tetragonal ($P4/nmm$) phases were taken from the ICSD reference database⁴¹ for the initial structure generation. The occupancy of Se and Te in both systems is 50:50. For the partial occupancy simulation, the ab initio random searching structure (AIRSS)⁴² approach was employed to create possible suitable model structures for the chosen substitution in the $\text{Fe}_{64}\text{Se}_{32}\text{Te}_{32}$ matrix, along with VASP calculations. As a result, in the acquired AIRSS model, Mn replaces one Fe, and the structure is entirely relaxed. In this case, the theoretical sample composition ($\text{Fe}_{0.984}\text{Mn}_{0.0156}\text{Se}_{0.5}\text{Te}_{0.5}$) is nearly identical to the experimental composition ($\text{Fe}_{0.99}\text{Mn}_{0.01}\text{Se}_{0.5}\text{Te}_{0.5}$). The resulting structures are depicted in Figure 3. To get a better understanding of the relative stability, total energy *versus* unit cell volume (see Figure 4a) was calculated for both phases. Figure 4b shows the measured cell volume of $86.2 \text{ \AA}^3 \text{ f.u.}^{-1}$,

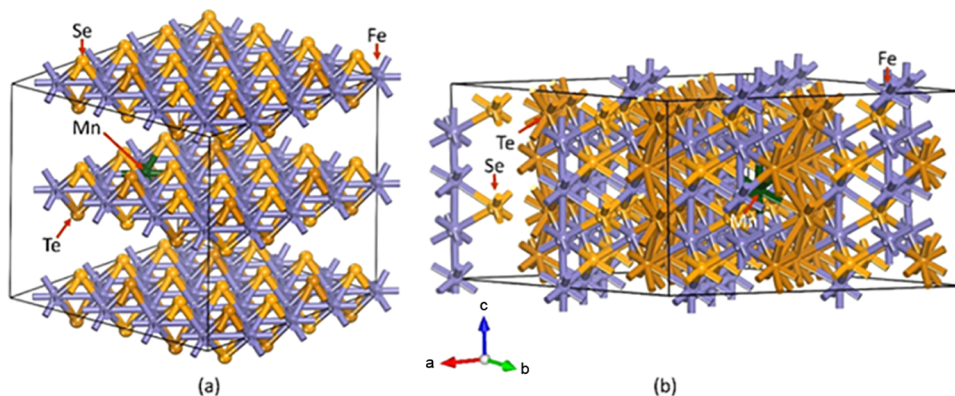


Figure 3. Considered low-energy structure model for $\text{Fe}_{0.984}\text{Mn}_{0.0156}\text{Se}_{0.5}\text{Te}_{0.5}$: (a) tetragonal structural phase ($P4/nmm$) at ambient conditions and (b) hexagonal ($P6_3/mmc$) structural phase at high pressure. Legends are notified for Fe, Mn, Se, and Te atoms.

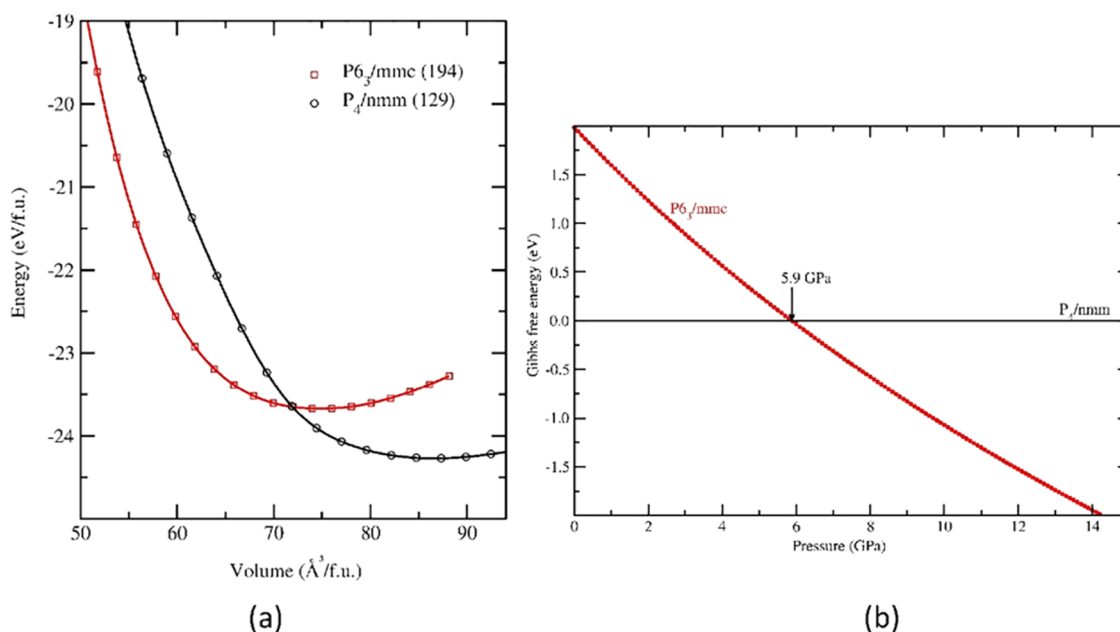


Figure 4. (a) Estimated volume dependence of total energy (a) and (b) stabilities of $P6_3/mmc$ relative to $P4/nmm$ as a function of pressure in $\text{Fe}_{0.984}\text{Mn}_{0.016}\text{Se}_{30}\text{Te}_{50}$. The transition pressure is marked by an arrow at the corresponding phase transition point.

and the tetragonal polymorph has the lowest energy structure, which is compatible with the experimental findings. Pressure-induced structural phase transformation from $P4/nmm$ to $P6_3/mmc$ was observed, and this entails reconstructive rearrangements of the cation and anion sublattices. The measured energy-volume data yields bulk module values of 36.8 and 95.3 GPa for $P4/nmm$ and $P6_3/mmc$, which agree well with experimental values of 33 and 80.7 GPa, respectively. Figure 5 shows the total density of states (DOS) for both $P4/nmm$

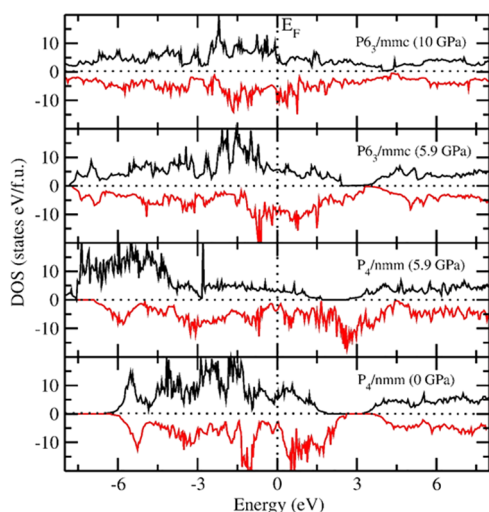


Figure 5. Estimated DOS as a function of energy at $P = 0$ GPa (for the tetragonal phase P_4/nmm) at higher P (where the transition occurs).

and $P6_3/mmc$ phases at equilibrium volumes and phase transition points. $P4/nmm$ has more electrons at Fermi energy (E_F) than $P6_3/mmc$. As P increases, the electron density increases at E_F in the tetragonal phase ($P4/nmm$) (see Figure 6). Despite the fact that $P6_3/mmc$ is not an energetically desirable structure in the pressure range 0–4 GPa, it exhibits a

similar tendency at E_F . This observation agrees with the experimental results that T_c decreases with increasing pressure due to a structural transition, together with a decrease in charge carriers in the density of states at the Fermi surface.

Heat Capacity Studies. Figure 7a shows the temperature-dependent heat capacity (C_p) measurement for $\text{Fe}_{0.99}\text{Mn}_{0.01}\text{Se}_{0.5}\text{Te}_{0.5}$ (inset) from 2 to 300 K without a magnetic field. There is a small heat capacity jump observed at $T_c = 14$ K showing the absence of bulk superconductivity. The T dependence of C_p can be explained by the Debye equation in the low-temperature region; the heat capacity behavior can be explained by the Debye equation⁴³ $C_p = \gamma T + \beta T^3 + CT^5$, where γ , β , and C are the electronic, lattice heat capacity, and anharmonic impurity contribution, respectively. Further, the equation well fits in the low-temperature region (Figure 7b) and gives fitting parameters of $\gamma = 25 \text{ mJ mol}^{-1} \text{ K}^{-2}$ and $\beta = 0.45 \text{ mJ mol}^{-1} \text{ K}^{-4}$; the estimated γ value is in agreement with the theoretical value.⁴⁴ The Debye temperature, $\Theta_D = (1944/\beta)^{1/3}$, estimated¹⁸ from the fitting parameter β is 162 K. $(C - \gamma T)/T^3$ vs T shows a broad maximum at $T_{\text{max}} \approx 13$ K. This characteristic temperature is described as the Einstein temperature, $\Theta_E \approx 4.92 T_{\text{max}}$ and it is estimated to be $\Theta_E \approx 64$ K. We analyzed the results using the MM theory⁴⁴ and showed that $\text{Fe}_{0.99}\text{Mn}_{0.01}\text{Se}_{0.5}\text{Te}_{0.5}$ samples fall under the phonon-mediated SC mechanism and T_c can be described as

$$T_c = \frac{\theta_D}{1.45} \exp \left[-\frac{1.04(1 + \lambda)}{\lambda - \mu^*(1 + 0.62\lambda)} \right] \quad (2)$$

where Θ_D , λ , and μ^* are the Debye temperature, the electron–phonon coupling constant, and the Coulomb pseudo-potential, respectively, and λ is estimated to be 1.12. Hence, the superconductivity for $\text{Fe}_{0.99}\text{Mn}_{0.01}\text{Se}_{0.5}\text{Te}_{0.5}$ could be understood based on the strong-coupling BCS theory as in the cases of $\text{FeSe}_{0.88}$ and $\text{FeSe}_{0.5}\text{Te}_{0.5}$,⁴⁵ where the estimated λ values were greater than 1.

Transport Properties under Pressure up to 8 GPa. The temperature-dependent resistance measurement, $R(T)$, of

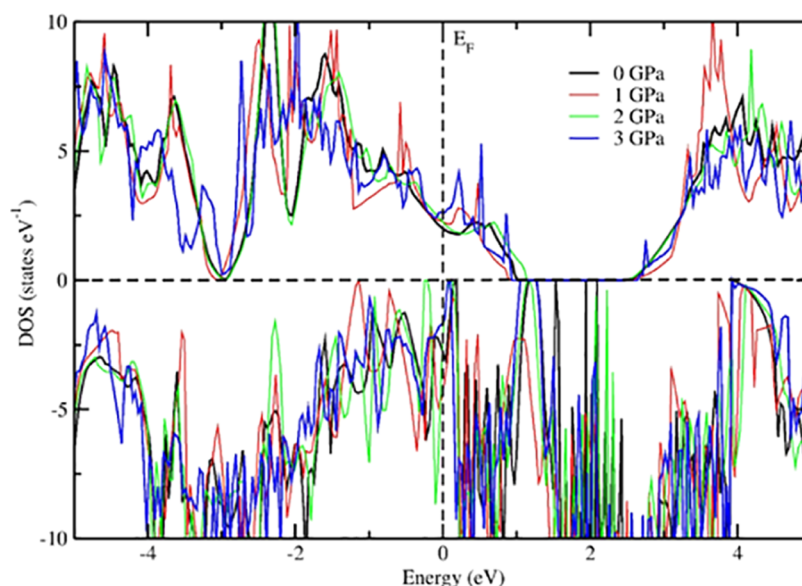


Figure 6. Calculated pressure dependence of the total density of states for the tetragonal phase (P_4/nmm), and the Fermi level is set at zero energy.

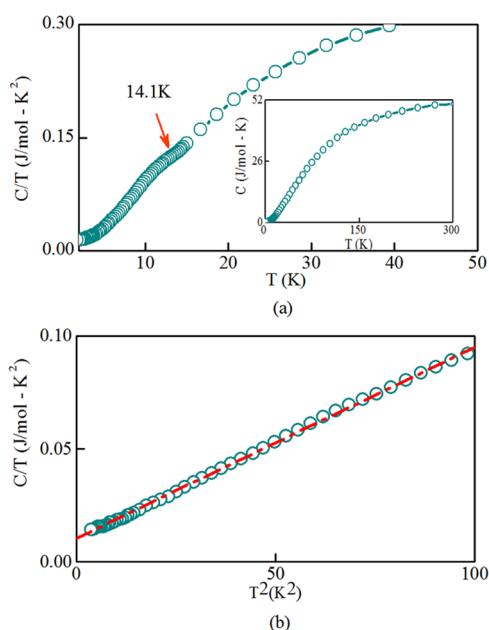


Figure 7. (a) Temperature dependencies of heat capacity, C_p , for $\text{Fe}_{0.99}\text{Mn}_{0.01}\text{Se}_{0.5}\text{Te}_{0.5}$ (inset; C_p from 300 to 2 K temperature). (b) C_p/T versus T^2 (2–100 K).

the $\text{Fe}_{0.99}\text{Mn}_{0.01}\text{Se}_{0.5}\text{Te}_{0.5}$ sample was measured using different types of pressure cells with various fixed pressures up to 10 GPa using a hybrid clamp-type piston cylinder pressure cell (3 GPa), DAC (5 GPa), and a cubic anvil press (10 GPa), shown, respectively, in (a), (b), and (c) of Figure 8. At ambient pressure, $R(T)$ results show a little increase of resistance as T decreases from 300 to 200 K, which indicates the semimetallic behavior of the sample. However, the resistance decreases from 200 to 14.1 K, which indicates the metallic behavior; further decrease of the temperature resistance suddenly drops to zero at $T_c = 14.1$ K, and it is consistent with the measured magnetization data and reported value.⁴⁶ The behavior of normal state resistance is similar to that of $\text{FeSe}_{0.5}\text{Te}_{0.5}$.^{47,48} However, it is to be noted that the resistance curve gets flattened at the same time as doping of Co and Ni at the Fe site

in $\text{FeSe}_{0.5}\text{Te}_{0.5}$ and T_c also gets decreased for Co ($T_c = 7$ K) and Ni ($T_c = 5.2$ K).⁴⁷ The significantly large overlap between electron and hole bands at the Fermi surface modifying the density of the charge carrier reflects the curved nature above T_c .⁴⁸ Further, on increasing P (>3 GPa), the resistance curves were flattened and the T_c increased monotonically from 14.1 to 22 K. The P dependence of T_c (P – T_c phase diagram) obtained from the $R(T)$ measurement under various P s was found to be domelike. Figure 8a–c clearly reveals that T_c was enhanced up to a P of ~ 3 GPa, at which it reached the highest T_c of 22 K and a positive temperature coefficient of $dT_c/dP = +2.6$ K/GPa (P range $0 \leq P \leq 3$ GPa). At higher P 's, T_c begins to turn down and the pressure coefficient becomes negative ($dT_c/dP = -3.6$ K/GPa ($3 \leq P \leq 9$ GPa)). Further, application of high P to 10 GPa leads to favoring the suppression of superconductivity. The phase diagram of T_c – P for $\text{Fe}_{0.99}\text{Mn}_{0.01}\text{Se}_{0.5}\text{Te}_{0.5}$ shown in Figure 9 reveals a change in the sign of the pressure coefficient from positive to negative that occurs at 3 GPa. A similar domelike behavior has been reported in FeSe and $\text{Fe}_{1.03}\text{Se}_{0.43}\text{Te}_{0.57}$ with maximum T_c values of 36 and 26 K,^{32,34,38} respectively.

Understanding the dome-shaped T_c – P phase diagram is challenging to have a deeper look into the mechanism of superconductivity in these materials. Effect of P on the FeSe system by varying the unit cell parameters interlayer/intralayer and interatomic distance⁴⁰ leads to modification of the electronic structure and strengthens the interaction among the electrons in the unit cells and the SC state affected by these parameters.

There are other possible reasons for the behavior of T_c . (i) At modest P until 4.5 GPa, an increase in $N(E_F)$ enhances the superconductivity and reaches a high T_c (22 K at 3 GPa in $R(T)$); however, at high P (>5 GPa), the lattice stiffening effect becomes detrimental to T_c or the P response of volume markedly changes at 3–4 GPa, revealing the structural distortion, which leads to a decrease in T_c . (ii) The $\text{Fe}_{0.99}\text{Mn}_{0.01}\text{Se}_{0.5}\text{Te}_{0.5}$ exhibits a partial structural phase transition (tetragonal to hexagonal phase), which reveals either an enhancement of the lattice stiffening or a transformation to a high-pressure phase, and charge carriers are reduced in the

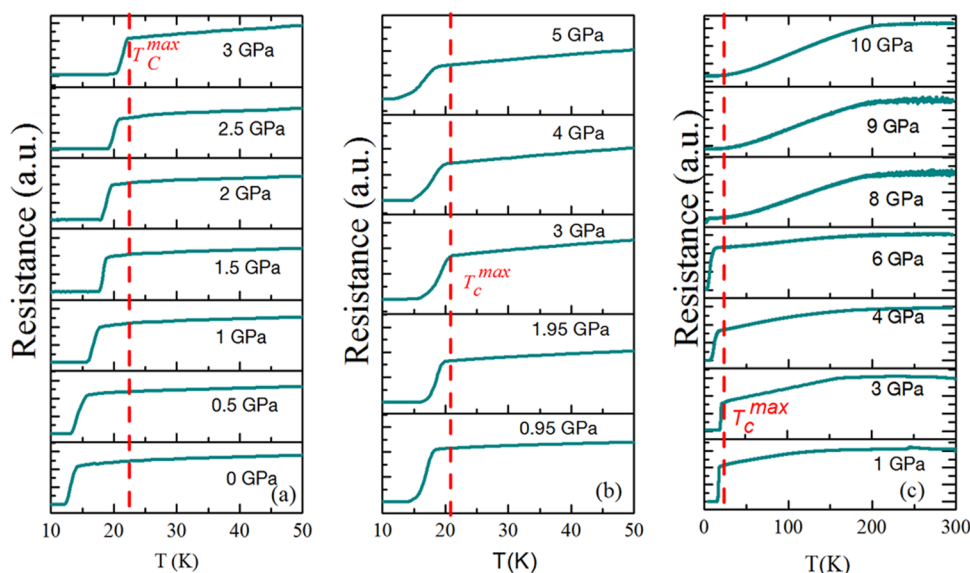


Figure 8. Temperature-dependent resistance (a) under $P \sim 3$ GPa (hybrid hydrostatic piston cylinder pressure cell), (b) up to 5 GPa (DAC), and (c) up to 10 GPa (cubic anvil press).

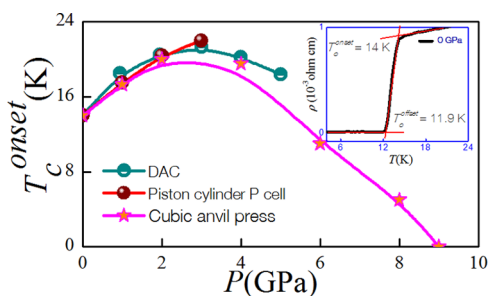


Figure 9. T_c extracted from resistance measurements, $R(T)$, under various pressures. The red one is from $R(T)$ measurement using a piston cylinder P cell, the dark-gray one is from $R(T)$ measurement using the diamond anvil cell, and the pink one is from $R(T)$ measurement using the cubic anvil press. (Inset: $R(T)$ measurement at 0 GPa, which shows the determined T_c s).

DOS in the Fermi surface, hence resulting in a decreased T_c . For the case of the $\text{Fe}_{0.99}\text{Ni}_{0.01}\text{Se}_{0.5}\text{Te}_{0.5}$ sample, the decrease of T_c due to the structural transition leads to the reduction of charge carriers in DOS on the Fermi surface.³⁹ For FeSe and $\text{FeSe}_{0.5}\text{Te}_{0.5}$, the observed T_c increase seems to be caused by the pressure-induced changes in the tetragonal phase and the imperfect Fermi surface nesting of corrugated cylinders, which

enhanced with increasing P , leading to higher values of T_c . The hybridization of Fe 3d electrons with chalcogenide 3p/4p states concurrently increases the DOS at the Fermi level [from 1.49 and 1.73 eV^{-1} (@ 0 GPa) to 1.54 eV^{-1} (@ ~ 9 GPa) and 1.77 eV^{-1} (@ 2 GPa) for FeSe and $\text{FeSe}_{0.5}\text{Te}_{0.5}$, respectively] under P , thus improving the SC properties.⁴⁹

Magnetic Properties under Pressure up to ~ 1.2 GPa.

Figure 10a shows the temperature dependence of magnetization ($M(T)$) at various pressures for the sample $\text{Fe}_{0.99}\text{Mn}_{0.01}\text{Se}_{0.5}\text{Te}_{0.5}$. At $P = 0$, bulk superconductivity is observed with the T_c onset of 13.5 K (see the inset of Figure 10a). Figure 10b shows two kinds of T_c (onset, offset) with respect to the applied P up to 1.2 GPa. The offset of T_c is almost consistent with the offset T_c of ~ 14.1 K in $R(T)$ measurements. The T_c increased monotonically from 13.9 to 19.1 K having a positive P coefficient of $dT_c/dP = +4.6$ K/GPa. The initial positive P coefficient is ~ 4.5 K/GPa ($T_c = 11$ K @ 0 GPa), and the highest T_c of 17 K was achieved at 1.2 GPa for $\text{Fe}_{0.97}\text{Co}_{0.03}\text{Fe}_{0.5}\text{Te}_{0.5}$;³⁶ a similar nature has been reported for $\text{FeSe}_{0.5}\text{Te}_{0.5}$ ⁵⁰ and $\text{FeSe}_{0.88}$.⁵¹ These same behaviors of the positive P coefficient were observed in Fe-based high-temperature superconductors.

Figure 11a–c shows the isothermal magnetization curves ($M[H]$) at different temperatures of the $\text{Fe}_{0.99}\text{Mn}_{0.01}\text{Se}_{0.5}\text{Te}_{0.5}$

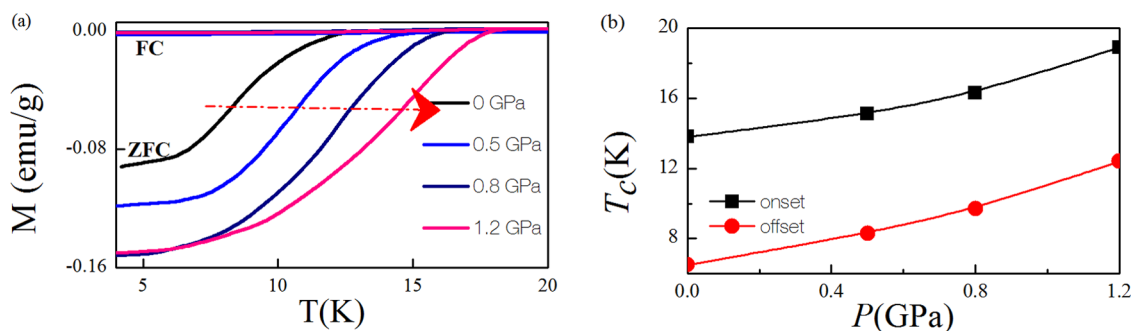


Figure 10. (a) $M(T)$ under various fixed hydrostatic pressures up to ~ 1.2 GPa (inset for ambient pressure to determine the superconducting transition temperatures T_c^{onset} , T_c^{offset}). (b) T_c versus pressure up to 1.2 GPa for $\text{Fe}_{0.99}\text{Mn}_{0.01}\text{Se}_{0.5}\text{Te}_{0.5}$.

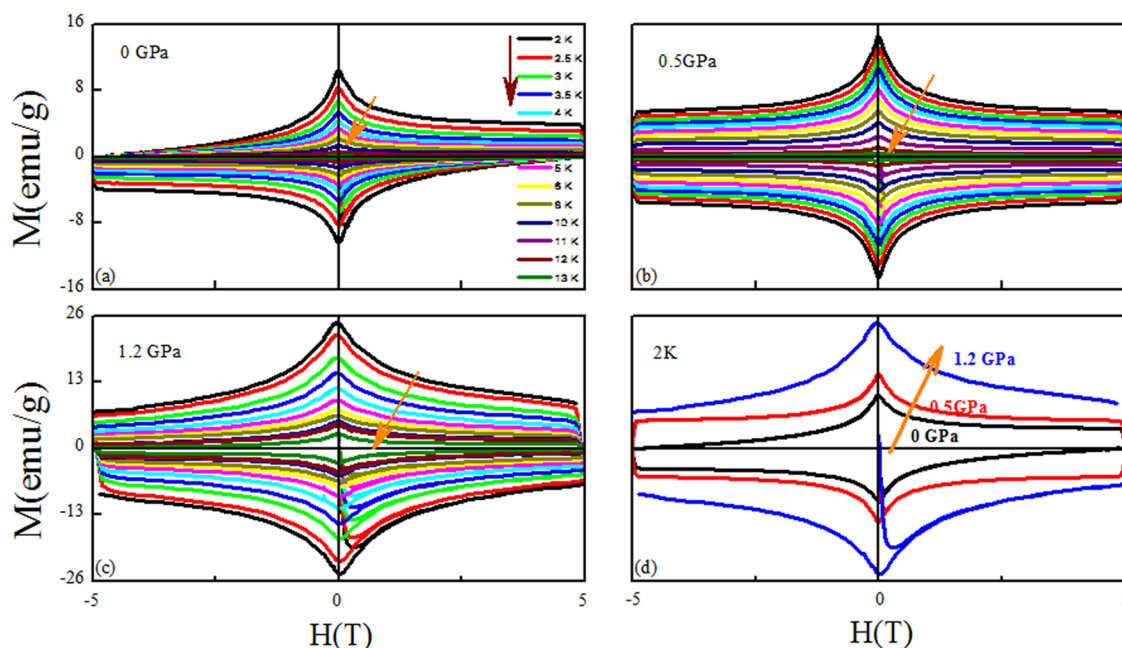


Figure 11. Isothermal magnetization curves, $M(H)$, for various temperatures 2, 2.5, 3, 4, 5, 6, 8, 10, 11, 12, and 13 K at (a) 0 GPa, (b) 0.5 GPa, and (c) 1.2 GPa of (d) field-dependent critical current density, $J_c(H)$, at 2 K under ambient, 0.5, and 1.2 GPa pressures for $\text{Fe}_{0.99}\text{Mn}_{0.01}\text{Se}_{0.5}\text{Te}_{0.5}$.

sample under 0, 0.5, and 1.2 GPa, respectively. A clear diamagnetic signal can be seen, suggesting a typical type II superconducting nature for all of the temperatures below T_c . Figure 11d shows the $M[H]$ curves at 2 K under 0, 0.5, and 1.2 GPa, and it reveals the enhancement of SC. From the $M(H)$ plot, we measured a lower critical field of $H_{c1} = 450$ Oe at 2 K for ambient pressure, and it was found to increase with P . For evaluating $H_{c1}(0)$ at zero temperature, we measured H_{c1} for P of 0, 0.5, and 1.2 GPa using the relation $H_{c1}(T) = H_{c1}(0)[1 - (T/T_c)^2]$ (not shown here); extrapolated $H_{c1}(0)$ values are 518, 563, and 617 Oe, respectively, for 0, 0.5, and 1.2 GPa. Further, the large opening of the $M(H)$ plot until 5 Tesla reveals the high H_{c2} for $\text{Fe}_{0.99}\text{Mn}_{0.01}\text{Se}_{0.5}\text{Te}_{0.5}$ at 2 K for all pressures. The values of H_{c2} were obtained from the field-dependent $R(T)$ for all of the applied pressures as shown in the inset of Figure 12, and it reveals the positive effect of P on the H_{c2} value similar to the Co-doped sample.³⁶ $H_{c2}(0)$ is obtained through the Werthamer–Helfand–Hohenberg (WHH) equation $H_{c2}(0) = -0.693T_c(dH_{c2}/dT)_{t=T_c}$. In Figure 12, the red line indicates the extrapolation of the Ginzburg–Landau formula $H_{c2}(T) = H_{c2}(0)(1 - t^2/1 + t^2)$, where $t = T/T_c$

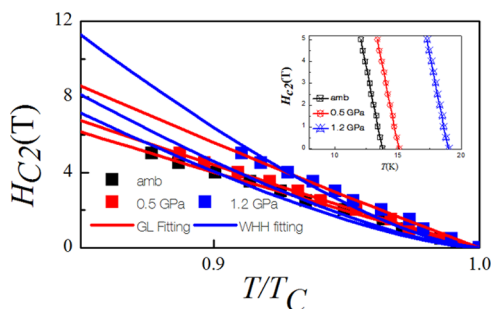


Figure 12. G – L and WHH fittings of the upper critical field $H_{c2}(T)$ versus normalized temperature T/T_c at ambient, 0.5, and 1.2 GPa pressures. Inset: $H_{c2}(T)$ vs temperature at ambient, 0.5, and 1.2 GPa pressures for $\text{Fe}_{0.99}\text{Mn}_{0.01}\text{Se}_{0.5}\text{Te}_{0.5}$.

and the blue line corresponds to the WHH equation. Obviously, the calculated $H_{c2}(0)$ values (given in Table 1)

Table 1. Superconducting Parameters under Pressure up to 1.2 GPa for $\text{Fe}_{0.99}\text{Mn}_{0.01}\text{Se}_{0.5}\text{Te}_{0.5}$

pressure (GPa)	$H_{c1}(0)$ (mT)	$H_{c2}(0)$ (T)	$\xi(0)_{\text{GL}}$ (Å)	κ	$\lambda(0)$ (Å)	$H_p(0)$ (T)
0	51.8	88.5	19.2	29.2	563	24.84
0.5	56.3	109	17.3	31.1	540	27.8
1.2	61.7	124	16.2	31.7	516	35

exceed the Pauli paramagnetic limit of $1.84T_c$, suggesting that $\text{Fe}_{0.99}\text{Mn}_{0.01}\text{Se}_{0.5}\text{Te}_{0.5}$ shows a heavy pinning or exotic nature. The G – L coherence length is calculated from the relation $\xi(0) = [\varphi_0/2\pi H_{c2}(0)]^{1/2}$, where φ_0 is defined as a flux quantum ($\varphi_0 = 2.0678 \times 10^{-15}$ T·m²). The calculated $\xi(0)$ at zero temperature at ambient P is comparable to the value reported for Cr¹⁸ and Co-doped samples,²⁷ and the obtained values of $\xi(0)$ for all pressures are given in Table 1.

The thermodynamic critical field $H_c(0)$ is calculated by the formula $H_c(0) = (H_{c1} * H_{c2})^{1/2}$, where H_{c1} and H_{c2} are the lower and upper critical fields at zero temperature. Further, the thermodynamic field and the upper critical field are connected by the relation $H_{c2} = 2^{1/2}\kappa H_c$, where κ is the kappa factor, also called the G – L parameter according to the Ginzburg–Landau theory, and the calculated κ values are 29.23, 31.11, and 31.7 for 0, 0.5, and 1.2 GPa, respectively. Such a large value ($>1/\sqrt{2}$) indicates that the type II SC is exhibited in $\text{Fe}_{0.99}\text{Mn}_{0.01}\text{Se}_{0.5}\text{Te}_{0.5}$. Further, for Co-doped⁵² (33.6) and Fe-chalcogenide SCs, the κ value lies in the same line. The London penetration depth $\lambda(0)$ is obtained through the equation $\lambda(0) = \kappa\xi(0)$, and it is found to be 563 Å for the ambient condition, comparable to 616 Å for the Co-doped⁵² one, and $\lambda(0)$ values for all of the applied P are given in Table 1.

The critical current density, J_c (A/cm²), is calculated from Bean’s critical state model $J_c = 20 \Delta M/[a(1 - (a/3b))]$,

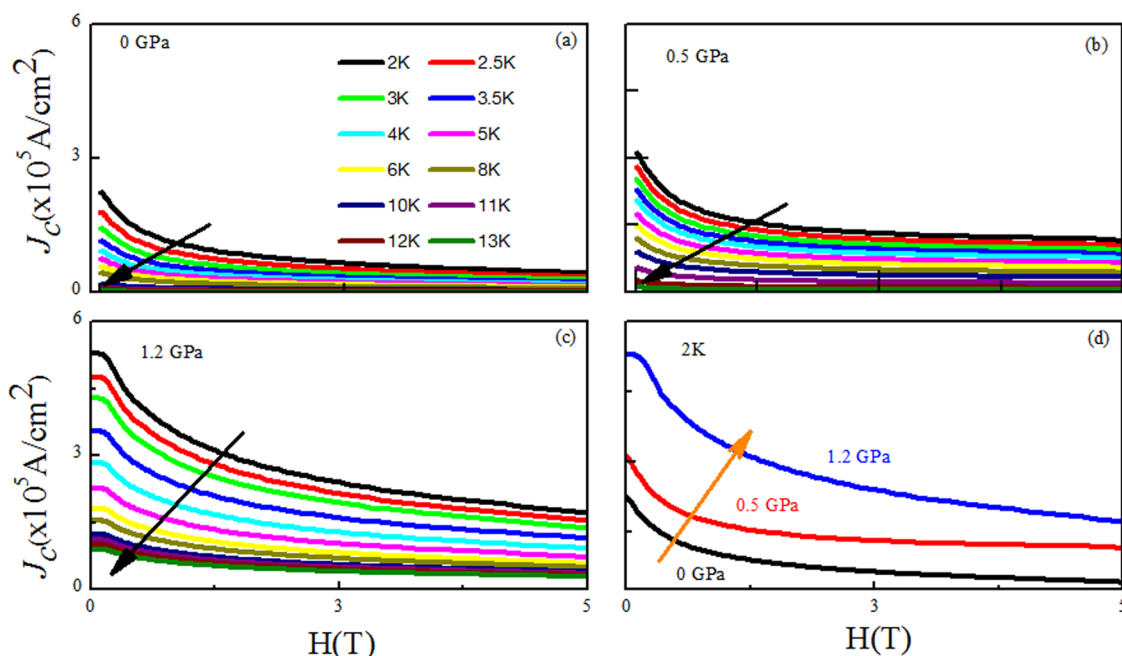


Figure 13. Field-dependent critical current density, $J_c(H)$, for various temperatures 2, 2.5, 3, 4, 5, 6, 8, 10, 11, 12, and 13 K at (a) ambient, (b) 0.5 GPa, and (c) 1.2 GPa pressures of $\text{Fe}_{0.99}\text{Mn}_{0.01}\text{SeTe}_{0.5}\text{e}_{0.5}$. (d) Field-dependent critical current density, $J_c(H)$, at 2 K under ambient, 0.5, and 1.2 GPa pressures.

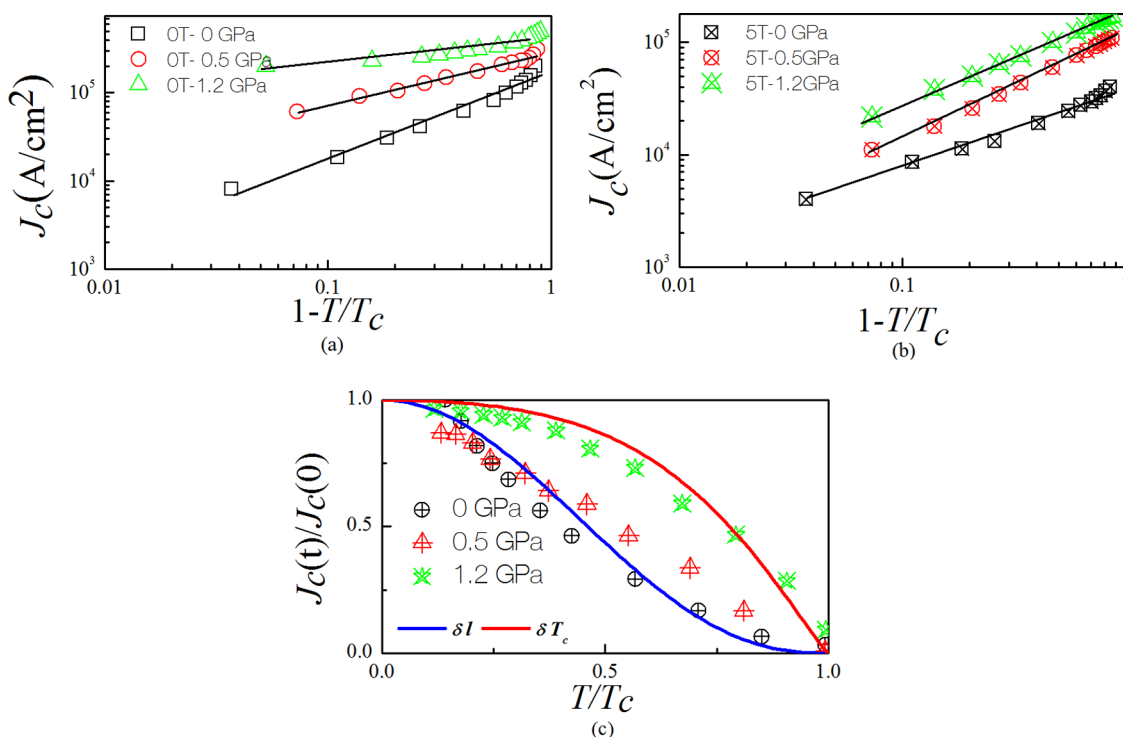


Figure 14. (a) Double logarithmic plot of J_c versus $(1 - T/T_c)$ at 0 T and (b) for 5 T under various pressures of 0, 0.5, and 1.2 GPa for $\text{Fe}_{0.99}\text{Mn}_{0.01}\text{Se}_{0.5}\text{Te}_{0.5}$; (c) $J_c(t)/J_c(0)$ versus T/T_c under various pressures for $\text{Fe}_{0.99}\text{Mn}_{0.01}\text{Se}_{0.5}\text{Te}_{0.5}$, in good agreement with δl and δT_c pinning.

where ΔM , a , and b are the difference in the magnetization, the width, and the thickness of the used sample, respectively.^{53,54} Field-dependent $J_c(H)$ plots for $\text{Fe}_{0.99}\text{Mn}_{0.01}\text{Se}_{0.5}\text{Te}_{0.5}$ at various temperatures for 0, 0.5, and 1.2 GPa are shown in Figure 13a–c, and d shows the $J_c(H)$ at 2 K for 0, 0.5, and 1.2 GPa. A strong enhancement of $J_c(H)$ is observed at both low and high fields. At 2 K, the low-field J_c is $\sim 2 \times 10^5$ A/cm² at 0 GPa, $\sim 3 \times 10^5$ A/cm² at 0.5 GPa, and $\sim 5 \times 10^5$ A/cm² at 1.2

GPa; the high-field J_c is also enhanced from 4×10^4 to 17×10^4 A/cm². The significant enhancement of J_c at high field and high temperature by P leads to the improvement of in-field performance. The highest J_c at 1.2 GPa for 2 K is higher than that of $\text{Fe}_{0.97}\text{Co}_{0.03}\text{Se}_{0.5}\text{Te}_{0.5}$ at both low fields and high fields.²⁷ The observed critical current densities $J_c(0)$ are ≈ 5000 and 15000 A/cm² at 6 K for $\text{FeSe}_{0.5}\text{Te}_{0.5}$ and $\text{Fe}_{0.97}\text{Co}_{0.03}\text{Se}_{0.5}\text{Te}_{0.5}$, respectively.²⁷ The irreversible fields (H_{irr}) of 0, 0.5, and 1.2

GPa are determined from the $M-H$ loop using the criteria of the zero critical current density, $J_c(0)$, because of depinning of the magnetic flux lines,⁵⁵ and it was found that H_{irr} increases with P .

Pinning Mechanism. From Figure 11d, when compared to the loop at $P = 0$ GPa, $M-H$ loops under P are significantly widened at both low and high fields, suggesting that the widening can be attributed to a huge enhancement of flux pinning under P .²⁷ To differentiate vortex pinning mechanisms in $\text{Fe}_{0.99}\text{Mn}_{0.01}\text{Se}_{0.5}\text{Te}_{0.5}$, the Ginzburg–Landau theory is employed. Based on the theory, J_c obeys the power law $J_c \propto (1 - T/T_c)^\beta$, where $\beta > 1.5$ for effective and strong vortex core pinning and $\beta = 1$ for individual, noninteracting vortices.^{56,57} Figure 14a,b shows the double logarithmic J_c versus $(1 - T/T_c)$, and β is 2.4–1.6 at 0 T and 4.5–2.3 at 5 T, indicating that this sample exhibits a strong and effective core pinning mechanism. Further, ambient and high-pressure data were analyzed by the collective pinning model. In general, two types of pinning mechanisms are known, i.e., δl and δT_c pinning mechanisms, and the observed results obey the following relations

$$\delta T_c \text{ pinning: } J_c(t)/J_c(0) = (1 - t^2)^{7/6}(1 + t^2)^{-6/5} \quad (3)$$

$$\delta l \text{ pinning: } J_c(t)/J_c(0) = (1 - t^2)^{5/2}(1 + t^2)^{-1/2} \quad (4)$$

where $t = T/T_c$, and $J_c(t)$ and $J_c(0)$ values were determined from the field-dependent J_c plots. Further, the normalized values, $J_c(t)/J_c(0)$, are plotted in Figure 14c. By fitting eqs 3 and 4 of the collective pinning model, the behavior of J_c is well described by the δl pinning mechanism at 0 GPa, which is because of changes in the mean free path l (δl), and by the δT_c pinning mechanism at 1.2 GPa, which is due to the spatial variation in the transition temperature for $\text{Fe}_{0.99}\text{Mn}_{0.01}\text{Se}_{0.5}\text{Te}_{0.5}$.

The pinning force ($F_p = J_c \times H$) versus field was calculated under various temperatures below T_c . It was found that the F_p value for this compound was enhanced significantly by P compared with the ambient condition. As P increased, the number of point pinning centers increased, resulting in an increase of the total pinning force. To have a further understanding of the pinning of the magnetic fluxes, the field-dependent pinning force was calculated for various P values up to 1.2 GPa. Figure 15 shows the normalized pinning force f_p (F_p/F_{pmax}) versus normalized magnetic field h (H/H_{irr}) plot for various fixed P values, and we used the Dew–Hughes model for scaling,²⁵ i.e., $f_p \approx h^p(1 - h)^q$, where $p = 1/2$ and $q = 2$; moreover, $p = 1$ and $q = 2$ describe surface pinning and

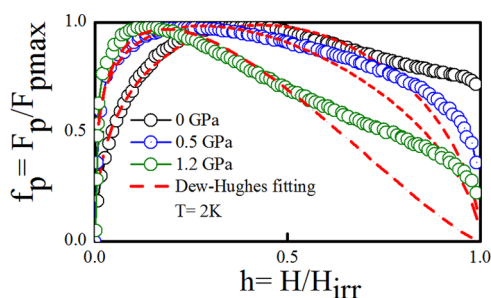


Figure 15. Normalized pinning force F_p/F_p^{\max} versus normalized field H/H_{irr} under various pressures 0, 0.5, and 1.2 GPa, in good agreement with the dense point pinning mechanism for the high pressure at 2 K.

point pinning, respectively.^{36,58–60} The experimental results show that the point pinning mechanism exhibits in $\text{Fe}_{0.99}\text{Mn}_{0.01}\text{Se}_{0.5}\text{Te}_{0.5}$ both at ambient and at P . The best fit of the curves is obtained with an $f(h)$ dependence given by $h^{1.3}(1 - h)^{2.7}$ for $P = 1.2$ GPa. The obtained $p = 1.3$ and $q = 2.7$ are similar to the observed values of $p = 1.35$ and 1.5 and $q = 3.06$ and 3.0 in $\text{Fe}_{1.04}\text{Te}_{0.6}\text{Se}_{0.4}$ ⁶⁰ and $\text{Fe}_{0.99}\text{Co}_{0.01}\text{Se}_{0.5}\text{Te}_{0.5}$,³⁶ respectively. In the Dew–Hughes model, it should be noted that $h_{\max} (=p/(p + q)) = 0.20$ and 0.33 correspond to surface pinning and point core pinning, respectively, for a normal center of core interaction. In the case of $\text{Fe}_{0.99}\text{Mn}_{0.01}\text{Se}_{0.5}\text{Te}_{0.5}$ under pressure, h_{\max} is 0.32 , and it corresponds to small-size normal point pinning.

Further, the matching field, where the defect spacing matches the vortex lattice spacing, gradually increases with increasing pressure as in the case of the $\text{Fe}_{0.99}\text{Co}_{0.01}\text{Se}_{0.5}\text{Te}_{0.5}$ ³⁶ sample in which the field-dependent intervortex distance decreases, consequently showing that the defect density increases with increasing pressure. Therefore, more point defects are expected under pressure in the $\text{Fe}_{0.99}\text{Mn}_{0.01}\text{Se}_{0.5}\text{Te}_{0.5}$ sample.

The maximum T_c of $\text{Fe}_{0.99}\text{Mn}_{0.01}\text{Se}_{0.5}\text{Te}_{0.5}$ is 22 K, while that of the $\text{Fe}_{0.99}\text{Ni}_{0.01}\text{Se}_{0.5}\text{Te}_{0.5}$ sample is 30.5 K up to 3 GPa, and the behavior of $R(T)$ data to low temperature also reveals a different behavior. The Mn-doped sample exhibits a low-temperature metallic behavior, $T < 140$ K ($T > 140$ reveals a semimetal nature), whereas the Ni-doped sample exhibits a low-temperature upturn $T < 100$ K, and at $T > 100$ K, it is metallic. However, the bulk and type II SC natures of Ni-doped samples with ferromagnetic backgrounds are not obvious; however, Mn-doped samples with $M-H$ loops without ferromagnetic backgrounds are fairly clear. The upper critical field is comparatively high for the Mn-doped sample. Hence, the Mn-doped sample is more preferred for practical applications than the Ni-doped sample. Further, structural studies for both systems show a tetragonal structure at ambient pressure and the mixed phase (tetragonal + hexagonal) is observed in the P region at ~ 7.5 – 14 and ~ 7.7 – 10 GPa for Ni- and Mn-doped samples, respectively. The DFT calculations show a higher electron density in $P4/nmm$ (ambient phase) than in $P6_3/mmc$ (high P phase), where the phase transition initiation for both samples is different (for Mn-doped sample: 5.9 GPa; for Ni-doped sample: 9.8 GPa). These high- P studies reveal that the Mn-doped sample reaches the high-pressure phase faster than the Ni-doped sample.

CONCLUSIONS

In conclusion, for $\text{Fe}_{0.99}\text{Mn}_{0.01}\text{Se}_{0.5}\text{Te}_{0.5}$, T_c attains a broad maximum of 22 K at ~ 3 GPa and then decreases. T_c is found to vanish at 9 GPa, where the pressure induces a structural phase transition from the tetragonal phase ($P4/nmm$) to the hexagonal phase ($P6_3/mmc$). This structural phase transition is expected to reduce the charge carrier in the density of states at the Fermi surface. The upper critical field is found to exceed the universal Pauli's limiting field, thus suggesting that an unconventional superconductivity mechanism is exhibited by this compound. These results prove that a considerable increase of the J_c value with the application of pressure reveals the enhancement of magnetic flux pinning. Interestingly, δl pinning is shown as a dominant pinning mechanism at 0 GPa and δT_c pinning at 1.2 GPa in $\text{Fe}_{0.99}\text{Mn}_{0.01}\text{Se}_{0.5}\text{Te}_{0.5}$. The normalized pinning force shows dense point pinning in this compound both at ambient pressure and under P .

Experimental Methods. Single crystals of $\text{Fe}_{0.99}\text{Mn}_{0.01}\text{Se}_{0.5}\text{Te}_{0.5}$ were grown by a self-flux melt growth method. High-purity (Alfa Aesar, 99.99%) Fe, Se, Te, and Mn powders were weighed, mixed in stoichiometric amounts, and ground thoroughly in an argon-filled glovebox. The procedure is the same as reported by Maheswari et al.⁶¹ The in situ powder X-ray diffraction method was performed under various P values up to 10 GPa at the Xpress beamline of the Elettra synchrotron radiation facility (Trieste, Italy).⁶² The wavelength and diameter of the synchrotron radiation used were ~ 0.4957 Å and ~ 50 μm , respectively, and the maximum P of 10 GPa was generated/applied using a gear-driven Boehler–Almax diamond anvil cell (DAC). The DAC is composed of a 500 μm paired culet. The sample chamber of the DAC was prepared by preindenting the gasket from 200 to ~ 110 μm thickness, and the center of the indented region was drilled by electrical discharge to a diameter of ~ 200 μm . Fine-ground powders were loaded inside the sample chamber to collect diffraction data to orientation effects. Silicone oil was used as a pressure-transmitting medium (PTM). Silicone oil is one of the common PTMs used in DAC for structural investigations due to its ease in managing the loading. Although hydrostatic conditions are not optimal when using silicone oil, it is found that even subtle structural anomalies can be observed with this PTM.⁶³ The pressure was calibrated using the shift in the ruby fluorescence techniques. A MAR-345 imaging plate detector was used for collecting the diffractograms. The data were collected from the imaging plate with an angular range between 4 and 30°, and fit2D software was employed to convert data into 2θ -intensity plots.⁶⁴ General Structure Analysis System (GSAS) software with the Rietveld method was used to refine the structural analysis.

Temperature dependence of electrical resistance ($R(T)$) was carried out for both ambient pressure and various hydrostatic pressures (up to ~ 3 GPa) down to 4 K temperature using the standard four-probe method using the clamp-type piston cylinder hybrid hydrostatic pressure cell and the physical property measurement system (PPMS Quantum Design).⁶⁵ Daphene oil (#7373) was used as an efficient pressure-transmitting medium (PTM) to maintain the hydrostaticity up to ~ 3 GPa. Bismuth (Bi) structural transition (I–II, II–III) under P at room temperature was used as a calibrant to estimate the actual pressure exhibits in the P cell. The onset of the superconducting transition temperature was determined using the criteria of inflection point of resistance marked where the two slopes intersect in $R(T)$ measurements.

The temperature dependence of heat capacity measurement from 300 to 4 K under ambient P was carried out using the physical property measurement system (Quantum), and $R(T)$ measurements under P (up to 5 GPa) were also carried out using 1000 μm culet diamond pairs and DAC at the Muroran Institute of Technology, Muroran Japan. A stainless steel gasket with thickness 300 μm was preindented to 100 μm , a miniature driller was used to make ϕ 200 μm at the center of the indentation, and fine powders of high-purity NaCl were used as PTMs. A small thin crystalline sample ($\sim 80 \times 20 \times 40$ μm^3) was placed on the NaCl medium, and the four contact leads were made by a 10 μm gold foil. The ruby fluorescence approach was used for monitoring the pressure in situ; two 5 μm ruby chips were placed along with the sample in the pressure cell. Pressure was measured at room temperature using the Ruby R1 line shift. $R(T)$ measurements up to ~ 12 GPa were done in the cubic anvil press at ISSP, Japan. As a

PTM, Daphene oil (#7474) was used to have a good hydrostatic P , and P calibration was carried out using bismuth (Bi) structural (I–II, II–III) transitions up to 5 GPa at room temperature. Four electrical contact leads were made on the $0.7 \times 0.4 \times 0.3$ mm^3 sample by a gold wire of ϕ 20 μm with high-quality silver paste.⁶⁶


Temperature-dependent DC magnetization ($M(T)$) was measured in ZFC and FC modes with a magnetic field of 10 Oe parallel to the c -axis of the single crystal in the temperature range from 20 to 2 K at ambient pressure and various hydrostatic P in a magnetic property measurement system (MPMS Quantum Design) and a hydrostatic piston cylinder pressure cell at ISSP Japan. A mixture of Fluorinert FC #77 and FC #70 with an equal ratio was used as a PTM. The in situ P in the piston cylinder P cell was estimated from the P dependence of T_c of pure Sn.⁶⁷ The critical current density, J_c , was determined from the field-dependent magnetization (M – H) data by the Bean model, $J_c = 20 \Delta M/[a(1 - (a/3b))]$, where ΔM , a , and b are the height difference in the M – H hysteresis loop, the width, and the length of the sample perpendicular to the applied field, respectively.

Theoretical Method. The projected-augmented plane-wave (PAW) method, as implemented in the Vienna ab initio simulation (VASP) package, was employed to perform DFT calculations.^{68,69} For crystal structure relaxation, the PBE (Perdew, Burke, and Ernzerhof)⁷⁰ functional was used, and for further simulations, the exchange-correlation functional with Hubbard parameter correction (GGA + U) was used.^{71,72} The Fe- d and Mn- d states were given as U values of 5.3 and 6.1 eV (with $J = 1$ eV), respectively. The conjugate-gradient algorithm with a force convergence threshold of 10^{-3} eV Å⁻¹ was used to estimate ground-state geometries by optimizing stresses and Hellman–Feynman forces. Throughout all relaxations, Brillouin zone integration was carried out with a Gaussian broadening of 0.1 eV, and the various sets of calculations revealed that 1152 k -points in the Brillouin zone for the structure with a 600 eV plane-wave cutoff were adequate to guarantee maximum accuracy in the computed values. For structural optimization, the k -point mesh was generated using the Monkhorst–Pack method with a grid size of $12 \times 12 \times 8$. To measure the total energy as a function of volume, a comparable density of k -points and energy cutoff was used for all of the structures considered in these calculations. Iteration was carried out for the relaxation of atomic positions until the variation of total energy less than 1 meV/cell was achieved between successive steps.

The volume-dependent total energy was calculated and fitted with the universal equation of state (EOS).⁷³ The Gibbs free energy vs pressure curves are often used to determine the transition pressures. The Gibbs free energy is obtained by fitting the total energy versus volume curve to the universal EOS equation. The P dependence of volume can be calculated using the formula (v) = $v_c/[(1 + (B_0^1/B_0) * P)^{1/B_0^1}]$, where v_c , B_0 , and B_0^1 denote the equilibrium volume, the bulk modulus, and its derivative with respect to P , respectively. The scan over the P values yields the change in enthalpy between two sets of data.

■ AUTHOR INFORMATION

Corresponding Author

Arumugam Sonachalam – Centre for High Pressure Research, School of Physics, Bharathidasan University, Tiruchirappalli 620024 Tamil Nadu, India;  orcid.org/0000-0002-2589-

7972; Phone: 91-431-2407118; Email: sarumugam1963@yahoo.com; Fax: 91-431-2407045

Authors

Kannan Murugesan – Centre for High Pressure Research, School of Physics, Bharathidasan University, Tiruchirappalli 620024 Tamil Nadu, India

Govindaraj Lingannan – Centre for High Pressure Research, School of Physics, Bharathidasan University, Tiruchirappalli 620024 Tamil Nadu, India

Kento Ishigaki – Institute for Solid state Physics, University of Tokyo, Kashiwa, Chiba 277-8581, Japan

Yoshiya Uwatoko – Institute for Solid state Physics, University of Tokyo, Kashiwa, Chiba 277-8581, Japan

Chihiro Sekine – Muroran Institute of Technology, Muroran, Hokkaido 050-8585, Japan

Yukihiro Kawamura – Muroran Institute of Technology, Muroran, Hokkaido 050-8585, Japan

Hayashi Junichi – Muroran Institute of Technology, Muroran, Hokkaido 050-8585, Japan

Boby Joseph – Elettra Sincrotrone Trieste ScPA, 34149 Trieste, Italy; orcid.org/0000-0002-3334-7540

Ponniiah Vajeeston – Department of Chemistry, Centre for Materials Science and Nanotechnology, University of Oslo, 0318 Oslo, Norway

Pankaj Kumar Maheswari – National Physical Laboratory (CSIR), New Delhi 110012, India

V. P. S. Awana – National Physical Laboratory (CSIR), New Delhi 110012, India; orcid.org/0000-0002-4908-8600

Complete contact information is available at:

<https://pubs.acs.org/10.1021/acsomega.1c03721>

Notes

The authors declare no competing financial interest.

ACKNOWLEDGMENTS

K.M. thanks CSIR for giving the meritorious fellowship (09/475(0200)/2018-EMR-I). A.S acknowledges DST-SERB (EMR/2016/006056), DST-FIST (SR/FST/PSI-204/2015(C)), DST –PURSE (SR/PURSE/PHASE 2/16 (C)), DST-JSPS (DST/INT/JSPS/P-26/7/2018), UGC-DAE (CSR-IC-MSRSR-04/CRS-2012/2017-18/1293), BRNS (58/14/06/2021-BRNS/37097), and TANSCH(RG/2019-20/BDU/HECP-0044). P.V. acknowledges the Research Council of Norway for providing the computer time (under project numbers NN2875k and NS2875k) at the Norwegian super-computer (Uninett Sigma2).

REFERENCES

- (1) Hsu, F.-C.; Luo, J.-Y.; Yeh, K.-W.; Chen, T.-K.; Huang, T.-W.; Wu, P.-M.; Lee, Y.-C.; Huang, Y.-L.; Chu, Y.-Y.; Yan, D.-C.; Wu, M.-K. Superconductivity in the PbO-type structure α -FeSe. *Proc. Natl. Acad. Sci. U.S.A.* **2008**, *105*, 14262–14264.
- (2) Bednorz, J. G.; Müller, K. A. Possible High T_c Superconductivity in the Ba-La-Cu-O System. *Z. Phys. B: Condens. Matter* **1986**, *64*, 189–193.
- (3) Wu, M. K.; Ashburn, J. R.; Torng, C. J.; et al. Superconductivity at 93 K in a New Mixed-Phase Y-Ba-Cu-O Compound System at Ambient Pressure. *Phys. Rev. Lett.* **1987**, *58*, No. 908.
- (4) Kamihara, Y.; Watanabe, T.; Hirano, M.; Hosono, H. Iron-based layered superconductor $\text{La}[\text{O}_{1-x}\text{F}_x]\text{FeAs}$ ($x = 0.05\text{--}0.12$) with $T_c = 26$ K. *J. Am. Chem. Soc.* **2008**, *130*, 3296–3297.

- (5) Rotter, M.; Tegel, M.; Johrendt, D. Superconductivity at 38 K in the iron arsenide $(\text{Ba}_{1-x}\text{K}_x)\text{Fe}_2\text{As}_2$. *Phys. Rev. Lett.* **2008**, *101*, No. 107006.

- (6) Ren, Z.-A.; Lu, W.; Yang, J.; Yi, W.; Shen, X.-L.; Li, Z.-C.; Che, G.-C.; Dong, X.-L.; Sun, L.-L.; Zhou, F.; Zhao, Z.-X. Superconductivity at 55 K in iron-based F-doped layered quaternary compound $\text{Sm}[\text{O}_{1-x}\text{F}_x]\text{FeAs}$. *Chin. Phys. Lett.* **2008**, *25*, 2215–2216.

- (7) Sang, L. N.; Lia, Z.; Yang, G. S.; Yu, Z. J.; Liu, J. X.; Cai, C. B.; Wu, T.; Dou, S. X.; Ma, Y. W.; Wang, X. L. Pressure effects on iron-based superconductor families: Superconductivity, flux pinning and vortex dynamics. *Mater. Today Phys.* **2021**, *19*, No. 100414.

- (8) Gajda, G.; Morawski, A.; Rogacki, K.; Cetner, T.; Zaleski, A. J.; Buchkov, K.; Nazarova, E.; Balchev, N.; Hossain, M. S. A.; Diduszko, R.; Gruszka, K.; Przystupski, P.; Gajda, D.; et al. Ag-doped $\text{FeSe}_{0.94}$ polycrystalline samples obtained through hot isostatic pressing with improved grain connectivity. *Supercond. Sci. Technol.* **2016**, *29*, No. 095002.

- (9) Wang, X. C.; Liu, Q. Q.; Lv, Y. X.; Gao, W. B.; Yang, L. X.; Yu, R. C.; Li, F. Y.; Jin, C. Q. The superconductivity at 18 K in LiFeAs system. *Solid State Commun.* **2008**, *148*, 538–540.

- (10) Wang, X.-L.; Ghorbani, S. R.; Lee, S.-I. K.; Dou, S. X.; Lin, C. T.; Johansen, T. H.; Cheng, Z. X.; Peleckis, G.; Müller, K.-H.; Shabazi, M.; Sun, G. L.; Sun, D. L. Very strong intrinsic supercurrent carrying ability and vortex avalanches in $(\text{Ba,K})\text{Fe}_2\text{As}_2$ superconducting single crystals. *Phys. Rev. B* **2010**, *82*, No. 024525.

- (11) Wang, X.; Ghorbani, S. R.; Peleckis, G.; Dou, S. Very High Critical Field and Superior Jc-Field Performance in $\text{NdFeAsO}_{0.82}\text{F}_{0.18}$ with T_c of 51 K. *Adv. Mater.* **2009**, *21*, 236–239.

- (12) Moll, P. J. W.; Puzniak, R.; Balakirev, F.; Rogacki, K.; Karpinski, J.; Zhigadlo, N. D.; Batlogg, B. High magnetic-field scales and critical currents in $\text{SmFeAs}(\text{O}, \text{F})$ crystals. *Nat. Mater.* **2010**, *9*, 628–633.

- (13) Ni, N.; Bud'ko, S. L.; Kreyssig, A.; Nandi, S.; Rustan, G. E.; Goldman, A. I.; Gupta, S.; Corbett, J. D.; Kracher, A.; Canfield, P. C. Anisotropic thermodynamic and transport properties of single-crystalline $\text{Ba}_{1-x}\text{K}_x\text{Fe}_2\text{As}_2$ ($x = 0$ and 0.45). *Phys. Rev. B* **2008**, *78*, No. 014507.

- (14) Wu, G.; Chen, H.; Wu, T.; Xie, Y. L.; Yan, Y. J.; Liu, R. H.; Wang, X. F.; Ying, J. J.; Chen, X. H. Different resistivity response to spin-density wave and superconductivity at 20 K in $\text{Ca}_{1-x}\text{Na}_x\text{Fe}_2\text{As}_2$. *J. Phys.: Condens. Matter* **2008**, *20*, No. 422201.

- (15) Athena, S. Sefat Pressure effects on two superconducting iron-based families. *Rep. Prog. Phys.* **2011**, *74*, No. 124502.

- (16) Fang, M. H.; Pham, H. M.; Qian, B.; Liu, T. J.; Vohstedt, E. K.; Liu, Y.; Spinu, L.; Mao, Z. Q. Superconductivity close to magnetic instability in $\text{Fe}(\text{Se}_{1-x}\text{Te}_x)_{0.82}$. *Phys. Rev. B* **2008**, *78*, No. 224503.

- (17) Yeh, K. W.; Huang, T. W.; Huang, Y. L.; Chen, T. K.; Hsu, F. C.; Wu, P. M.; Lee, Y. C.; Chu, Y. Y.; Chen, C. L.; Luo, J. Y.; Yan, D. C.; Wu, M. K. Tellurium substitution effect on superconductivity of the α -phase iron selenide. *Europhys. Lett.* **2008**, *84*, No. 37002.

- (18) Yadav, A. K.; Sanchela, A. V.; Tomy, C. V. Improvement of superconducting properties in $\text{Fe}_{1+x}\text{Se}_{0.5}\text{Te}_{0.5}$ superconductor by Cr-substitution. *Solid State Commun.* **2015**, *206*, 26–30.

- (19) Migita, M.; Takikawa, Y.; Sugai, K.; Takeda, M.; Uehara, M.; Kuramoto, T.; Takano, Y.; Mizuguchi, Y.; Kimishima, Y. Substitution effects of Ag into $\text{FeSe}_{0.5}\text{Te}_{0.5}$ superconductor. *Phys. C* **2013**, *484*, 66–68.

- (20) Chen, N.; Liu, Y.; Ma, Z.; Huijun, Li.; Shahriar Al Hossain, M. Enhancement of superconductivity in the sintered $\text{FeSe}_{0.5}\text{Te}_{0.5}$ bulks with proper amount of Sn addition. *J. Alloys Compd.* **2015**, *633*, 233–236.

- (21) Zhang, A. M.; Xia, T. L.; Kong, L. R.; Xiao, J. H.; Zhang, Q. M. Effects on superconductivity of transition-metal doping in $\text{FeSe}_{0.5}\text{Te}_{0.5}$. *J. Phys.: Condens. Matter* **2010**, *22*, No. 245701.

- (22) Zhang, Z. T.; Yang, Z. R.; Li, L.; Zhang, C. J.; Pi, L.; Tan, S.; Zhang, Y. H. Magnetism and superconductivity in $\text{M}_x\text{Fe}_{1+y}\text{Te}_{1-z}\text{Se}_z$ ($\text{M} = \text{Cr}, \text{Mn}, \text{Co}, \text{Ni}, \text{Cu}, \text{and Zn}$) single crystals. *J. Appl. Phys.* **2011**, *109*, No. 07E113.

- (23) Cieplak, M. Z.; Bezusyy, V. L. Transition metal doping of FeSeTe: what can we learn from transport properties. *Philos. Mag.* **2015**, *95*, 480–492.
- (24) Shipra, R.; Takeya, H.; Hirata, K.; Sundaresan, A. Effects of Ni and Co doping on the physical properties of tetragonal FeSe_{0.5}Te_{0.5} superconductor. *Phys. C* **2010**, *470*, 528–532.
- (25) Leo, A.; Grimaldi, G.; Guarino, A.; Avitabile, F.; Nigro, A.; Galluzzi, A.; Mancusi, D.; Polichetti, M.; Pace, S.; Buchkov, K.; Nazarova, E.; Kawale, S.; Bellingeri, E.; Ferdeghini, C. Vortex pinning properties in Fe chalcogenides. *Supercond. Sci. Technol.* **2015**, *28*, No. 125001.
- (26) Wu, Z. F.; Wang, Z. H.; Tao, J.; Qiu, L.; Yang, S. G.; Wen, H. H. Flux pinning and relaxation in FeSe_{0.5}Te_{0.5} single crystals. *Supercond. Sci. Technol.* **2016**, *29*, No. 035006.
- (27) Sang, L.; Maheswari, P.; Yu, Z.; Yun, F. F.; Zhang, Y.; Dou, S.; Cai, C.; Awana, V. P. S.; Wang, X. Point defect induced giant enhancement of flux pinning in Co-doped FeSe_{0.5}Te_{0.5} superconducting single crystals. *AIP Adv.* **2017**, *7*, No. 115016.
- (28) Mizuguchi, Y.; Takano, Y. Review of Fe Chalcogenides as the Simplest Fe-Based Superconductor. *J. Phys. Soc. Jpn.* **2010**, *79*, No. 102001.
- (29) Shabbir, B.; Wang, X.; Ma, Y.; Dou, S. X.; Yan, S. S.; Mei, L. M. Study of flux pinning mechanism under hydrostatic pressure in optimally doped (Ba,K)Fe₂As₂ single crystals. *Sci. Rep.* **2016**, *6*, No. 23044.
- (30) Gajda, D.; Morawski, A.; Zaleski, A.; Malecka, M.; Cetner, T.; Rogacki, K. Enhancement of pinning centers density and structure by using hot isostatic pressure of 1.2 GPa in Ba (Fe_{0.92}, Co_{0.08})₂As₂ superconducting material. *J. Alloys Compd.* **2017**, *726*, 1220–1225.
- (31) Medvedev, S.; McQueen, T. M.; Troyan, I. A.; Palasyuk, T.; Eremets, M. I.; Cava, R. J.; Naghavi, S.; Casper, F.; Ksenofontov, V.; Wortmann, G.; Felser, C. Electronic and magnetic phase diagram of β-Fe_{1.01}Se with superconductivity at 36.7 K under pressure. *Nat. Mater.* **2009**, *8*, 630–633.
- (32) Gresty, N. C.; Takabayashi, Y.; Ganin, A. Y.; McDonald, M. T.; Claridge, J. B.; Giap, D.; Mizuguchi, Y.; Takano, Y.; Kagayama, T.; Ohishi, Y.; Takata, M.; Rosseinsky, M. J.; Margadonna, S.; Prassides, K. Structural Phase Transitions and Superconductivity in Fe_{1+δ}Se_{0.57}Te_{0.43} at Ambient and Elevated Pressures. *J. Am. Chem. Soc.* **2009**, *131*, 16944–16952.
- (33) Mizuguchi, Y.; Tomioka, F.; Tsuda, S.; Yamaguchi, T.; Takano, Y. Superconductivity at 27K in tetragonal FeSe under high pressure. *Appl. Phys. Lett.* **2008**, *93*, No. 152505.
- (34) Margadonna, S.; Takabayashi, Y.; Ohishi, Y.; Mizuguchi, Y.; Takano, Y.; Kagayama, T.; Nakagawa, T.; Takata, M.; Prassides, K. Pressure evolution of the low-temperature crystal structure and bonding of the superconductor FeSe (T_c = 37 K). *Phys. Rev. B* **2009**, *80*, No. 064506.
- (35) Garbarino, G.; Sow, A.; Lejay, P.; Sulpice, A.; Toulemonde, P.; Mezouar, M.; Nunez-Regueiro, M. High-temperature superconductivity (T_c onset at 34 K) in the high-pressure orthorhombic phase of FeSe. *Europhys. Lett.* **2009**, *86*, 27001.
- (36) Sang, L.; Shabbir, B.; Maheswari, P.; Qiu, W.; Ma, Z.; Dou, S.; Cai, C.; Awana, V. P. S.; Wang, X. Hydrostatic pressure-induced huge enhancement of critical current density and flux pinning in Fe_{1-x}Co_xSe_{0.5}Te_{0.5} single crystals. *Supercond.Sci.Technol.* **2018**, *31*, No. 025009.
- (37) Braithwaite, D.; Salce, B.; Lapertot, G.; Bourdarot, F.; Marin, C.; Aoki, D.; Hanfland, M. Superconducting and normal phases of FeSe single crystals at high pressure. *J. Phys.: Condens. Matter* **2009**, *21*, 232202–232206.
- (38) Kumar, R. S.; Zhang, Y.; Sinogeikin, S.; Xiao, Y.; Kumar, S.; Chow, P.; Cornelius, A. L.; Chen, C. Crystal and Electronic Structure of FeSe at High Pressure and Low Temperature. *J. Phys. Chem. B* **2010**, *114*, 12597–12606.
- (39) Ganesan, K.; Lingannan, G.; Murugesan, K.; Perreault, C. S.; Samudrala, G. K.; Maheswari, P. K.; Awana, V. P. S.; Vajeeston, P.; Vohra, Y. K.; Arumugam, S. Pressure-induced structural transition and huge enhancement of superconducting properties of single-crystal Fe_{0.99}Ni_{0.01}Se_{0.5}Te_{0.5} unconventional superconductor. *J. Mater. Res.* **2021**, *36*, 1624–1636.
- (40) Katsura, T.; Tange, Y. A Simple Derivation of the Birch–Murnaghan Equations of State (EOSs) and Comparison with EOSs Derived from Other Definitions of Finite Strain. *Minerals* **2019**, *9*, 745.
- (41) Bergerhoff, G.; Hundt, R.; Sievers, R.; Brown, I. D. The inorganic crystal structure data base. *J. Chem. Inf. Comput. Sci.* **1983**, *23*, 66–69.
- (42) Chris, J. P.; Needs, R. J. Ab initio random structure searching. *J. Phys.: Condens. Matter* **2011**, *23*, No. 053201.
- (43) Sales, B. C.; Sefat, A. S.; McGuire, M. A.; Jin, R. Y.; Mandrus, D.; et al. Bulk superconductivity at 14 K in single crystals of Fe_{1+y}Te_xSe_{1-x}. *Phys. Rev. B* **2009**, *79*, No. 094521.
- (44) Kumar, S.; Singh, P. P. First-principles study of electronic and magnetic properties of Fe_{1-x}TM_xSe_{0.5}Te_{0.5} alloys (TM ≡ Cr, Mn, Co, Ni). *J. Alloys Compd.* **2016**, *663*, 295–310.
- (45) Huang, C.-L.; Chou, C.-C.; Tseng, K.-F.; Huang, Y.-L.; Hsu, F.-C.; Yeh, K.-W.; Wu, M.-K.; Yang, H.-D. Pressure Effects on Superconductivity and Magnetism in FeSe_{1-x}Te_x. *J. Phys. Soc. Jpn* **2009**, *78*, No. 084710.
- (46) Gunther, A.; Deisenhofer, J.; Kant, Ch.; Krug von Nidda, H.-A.; Tsurkan, V.; Loid, A. Improvement of superconducting properties of FeSe_{0.5}Te_{0.5} single crystals by Mn substitution. *Supercond. Sci. Technol.* **2011**, *24*, No. 045009.
- (47) Awana, V. P. S.; Pal, A.; Vajpayee, A.; Mudge, M.; Kishan, H.; Husain, M.; Zeng, R.; Yu, S.; Guo, Y. F.; Shi, Y. G.; Yamaura, K.; Takayama-Muromachi, E. Synthesis and physical properties of FeSe_{1/2}Te_{1/2} superconductor. *J. Appl. Phys.* **2010**, *107*, No. 09E128.
- (48) Shipra, R.; Takeya, H.; Hirata, K.; Sundaresan, A. Effects of Ni and Co doping on the physical properties of tetragonal FeSe_{0.5}Te_{0.5} superconductor. *Phys. C* **2010**, *470*, 528–532.
- (49) Ciecchan, A.; Winiarski, M. J.; Samsel-Czeka, M. The Pressure Effects on Electronic Structure of Iron Chalcogenide Superconductors FeSe_{1-x}Te_x. *Acta Phys. Pol., A* **2012**, *121*, No. 820.
- (50) Huang, C.-L.; Chou, C.-C.; Tseng, K.-F.; Huang, Y.-L.; Hsu, F.-C.; Yeh, K.-W.; Wu, M.-K.; Yang, H.-D. Pressure Effects on Superconductivity and Magnetism in FeSe_{1-x}Te_x. *J. Phys. Soc. Jpn.* **2009**, *78*, No. 084710.
- (51) Mizuguchi, Y.; Tomioka, F.; Tsuda, S.; Yamaguchi, T.; Takano, Y. Superconductivity at 27K in tetragonal FeSe under high pressure. *Appl. Phys. Lett.* **2008**, *93*, No. 152505.
- (52) Maheswari, P. K.; Gahtori, B.; Gupta, A.; Awana, V. P. S. Impact of Fe site Co substitution on superconductivity of Fe_{1-x}Co_xSe_{0.5}Te_{0.5} (x = 0.0 to 0.10): A flux free single crystal study. *AIP Adv.* **2017**, *7*, No. 015006.
- (53) Bean, C. P. Magnetization of Hard Superconductors. *Phys. Rev. Lett.* **1962**, *8*, 250–253.
- (54) Bean, C. P. Magnetization of High-Field Superconductors. *Rev. Mod. Phys.* **1964**, *36*, 31–39.
- (55) Shirage, P. M.; Tanaka, Y.; Iyo, A. The critical current density, irreversibility line, and flux pinning properties of Ba₂CaCu₂O₄ (O, F)₂ high-T_c superconductor. *J. Appl. Phys.* **2010**, *107*, No. 093905.
- (56) Bruck, S.; Albrecht, J. Experimental evidence of the dominant role of low-angle grain boundaries for the critical current density in epitaxially grown YBa₂Cu₃O_{7-δ} thin films. *Phys. Rev. B* **2005**, *71*, No. 174508.
- (57) Djupmyr, M.; Cristiani, G.; Habermeier, H. U.; Albrecht, J. Anisotropic temperature-dependent current densities in vicinal YBa₂Cu₃O_{7-δ}. *Phys. Rev. B* **2005**, *72*, No. 220507.
- (58) Kramer, E. J. Scaling laws for flux pinning in hard superconductors. *J. Appl. Phys.* **1973**, *44*, 1360–1370.
- (59) Pervin, R.; Krishnan, M.; Rana, A. K.; Kannan, M.; Arumugam, S.; Shirage, P. M. Enhancement of superconducting critical current density by Fe impurity substitution in NbSe₂ single crystals and the vortex pinning mechanism. *Phys. Chem. Chem. Phys.* **2017**, *19*, 11230–11238.
- (60) Shahbazi, M.; Wang, X. L.; Dou, S. X.; Fang, H.; Lin, C. T. The flux pinning mechanism, and electrical and magnetic anisotropy in

Fe_{1.04}Te_{0.6}Se_{0.4} superconducting single crystal. *J. Appl. Phys.* **2013**, *113*, No. 17E115.

(61) Sang, L.; Maheswari, P.; Yu, Z.; Yun, F. F.; Zhang, Y.; Dou, S.; Cai, C.; Awana, V. P. S.; Wang, X. Point defect induced giant enhancement of flux pinning in Co-doped FeSe_{0.5}Te_{0.5} superconducting single crystals. *AIP Adv.* **2017**, *7*, No. 115016.

(62) Lotti, P.; Milani, S.; Merlini, M.; Joseph, B.; Alabarse, F.; Lausi, A. Single-crystal diffraction at the high-pressure Indo-Italian beamline Xpress at Elettra, Trieste. *J. Synchrotron Rad.* **2020**, *27*, 222–229.

(63) Pillai, S. B.; Joseph, B.; Upadhyay, D.; Marini, C.; Jha, P. K. Pressure Induced Hydrogen Order–Disorder Transition in β -Ni(OH)₂. *Phys. Chem. C* **2021**, *125*, 2785–2792.

(64) Artini, C.; Massardo, S.; Carnasciali, M. M.; Joseph, B.; Pani, M. In Situ High Pressure Structural Investigation of Sm-Doped Ceria. *Energies* **2020**, *13*, 1558.

(65) Holzapfel, W. B.; Isaacs, N. S. *High-Pressure Techniques in Chemistry and Physics*; Oxford University Press, 1997.

(66) Mori, N.; Takahashi, H.; Takeshita, N. Low-temperature and high-pressure apparatus developed at ISSP, University of Tokyo. *High Press. Res.* **2004**, *24*, 225–232.

(67) Eiling, A.; Schilling, J. S. Pressure and temperature dependence of electrical resistivity of Pb and Sn from 1-300K and 0-10 GPa-use as continuous resistive pressure monitor accurate over wide temperature range; superconductivity under pressure in Pb, Sn and In. *J. Phys. F: Met. Phys.* **1981**, *11*, 623.

(68) Kresse, G.; Furthmüller, J. Efficient iterative schemes for ab initio total-energy calculations using a plane-wave basis set. *Phys. Rev. B.* **1996**, *54*, 11169–11186.

(69) Kresse, G.; Furthmüller, J. Efficiency of ab-initio total energy calculations for metals and semiconductors using a plane-wave basis set. *Comput. Mater. Sci.* **1996**, *6*, 15–50.

(70) Perdew, J. P.; Burke, K.; Ernzerhof, M. Generalized Gradient Approximation Made Simple. *Phys. Rev. Lett.* **1996**, *77*, 3865–3868.

(71) Liechtenstein, A. I.; Anisimov, V. I.; Zaanen, J. Density-functional theory and strong interactions. *Phys. Rev. B* **1995**, *52*, R5467–R5470.

(72) Dudarev, S. L.; Botton, G. A.; Savrasov, S. Y.; Szotek, Z.; Temmerman, W. M.; Sutton, A. P. Electronic Structure and Elastic Properties of Strongly Correlated Metal Oxides from First Principles: LSDA + U, SIC-LSDA and EELS Study of UO₂ and NiO. *Phys. Status Solidi A.* **1998**, *166*, 429–443.

(73) Vinet, P.; Rose, J. H.; Ferrante, J.; Smith, J. R. Universal features of the equation of state of solids. *J. Phys.: Condens. Matter* **1989**, *1*, 1941–1948.